

cuVSLAM: CUDA accelerated visual odometry and mapping

Alexander Korovko¹, Dmitry Slepichev¹, Alexander Efitorov¹, Aigul Dzhumamuratova¹, Viktor Kuznetsov¹, Joydeep Biswas¹, Hesam Rabeti¹ and Soha Pouya¹

¹NVIDIA, {akorovko, dslepichev, aefitorov, adzhumamurat, vkuznetsov, jbiswas, hrabeti, spouya}@nvidia.com

Abstract

Accurate and robust pose estimation is a key requirement for any autonomous robot. We present cuVSLAM, a state-of-the-art solution for visual simultaneous localization and mapping, which can operate with a variety of visual-inertial sensor suites, including multiple RGB and depth cameras, and inertial measurement units. cuVSLAM supports operation with as few as one RGB camera to as many as 32 cameras, in arbitrary geometric configurations, thus supporting a wide range of robotic setups. cuVSLAM is specifically optimized using CUDA to deploy in real-time applications with minimal computational overhead on edge-computing devices such as the NVIDIA Jetson. We present the design and implementation of cuVSLAM, example use cases, and empirical results on several state-of-the-art benchmarks demonstrating the best-in-class performance of cuVSLAM.

Acknowledgements

We would like to extend our heartfelt acknowledgment to Eugene Vendrovskiy, Stanislav Volodarskiy, and Dmitry Robustov for their invaluable contributions to this project. Their profound expertise, exceptional skills, and commitment to excellence have been pivotal in shaping the outcomes of this work.

1. Introduction

Visual Simultaneous Localization and Mapping (VSLAM) is a fundamental capability for autonomous robots, enabling them to build a metric map of their environment while simultaneously determining their location within it. The increasing deployment of autonomous robots across diverse applications, from warehouse automation to last-mile delivery, has created a pressing need for robust, real-time VSLAM solutions that can operate efficiently across diverse settings, while being able to run on energy-efficient edge computing devices.

Traditional VSLAM systems face several key challenges: they often struggle with real-time performance on resource-constrained platforms, have limited flexibility in sensor configurations, and may not fully utilize available hardware acceleration capabilities. Additionally, many existing solutions are optimized for specific sensor configurations, making them less adaptable to diverse robotic platforms with varying sensor requirements.

We evaluate cuVSLAM on standard benchmarks, demonstrating state-of-the-art accuracy while maintaining real-time performance on edge computing platforms. Our results show that cuVSLAM achieves average trajectory errors below 1% on the KITTI odometry benchmark and position errors under 5cm on the EuRoC dataset, while processing frames in real-time on NVIDIA Jetson platforms. Multi-Stereo mode significantly improves accuracy and robustness on challenging sequences compared to single stereo cameras, as validated through both simulated and real-world dataset evaluations.

We present cuVSLAM, a CUDA-accelerated visual SLAM system designed to address these challenges. cuVSLAM offers several key innovations:

- Flexible sensor suite support, accommodating configurations from a single RGB camera to complex arrays of up to 32 cameras with arbitrary geometric arrangements

- Support for optional IMU and depth sensors
- Efficient CUDA implementation enabling real-time performance on edge devices like NVIDIA Jetson
- A modular architecture separating frontend pose estimation from backend map refinement
- Robust feature tracking and mapping capabilities that maintain accuracy across diverse environments

Our technical approach combines classical SLAM techniques with modern GPU acceleration. The frontend module performs real-time pose estimation using feature detection, tracking, and local mapping, while the backend handles global map consistency through pose graph optimization and loop closure. By leveraging CUDA acceleration throughout the pipeline, from feature detection to bundle adjustment, cuVSLAM achieves superior performance while maintaining high accuracy.

The rest of this technical report is organized as follows: Section 2 describes the system architecture and design, Section 3 presents experimental results and benchmarks, and Section 4 concludes with discussion and future work.

2. System Architecture and Design

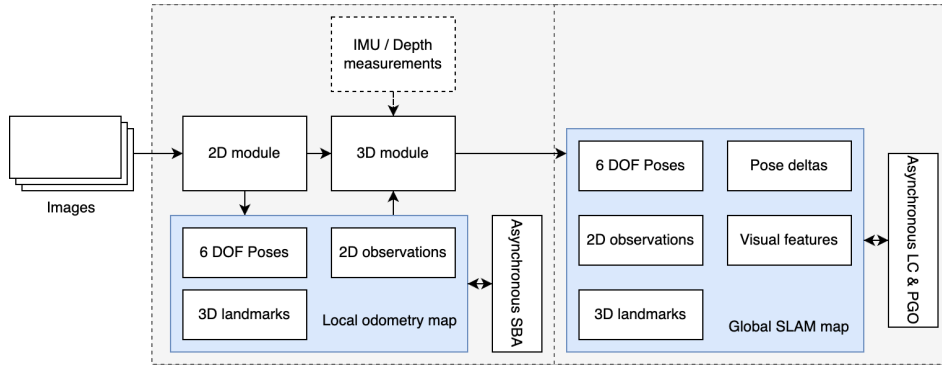


Figure 1: cuVSLAM architecture

The cuVSLAM library implements a general approach to camera pose estimation, where the architecture consists of two major blocks: the frontend, responsible for online pose estimation with minimal latency and maximum throughput, and the backend, focusing on asynchronous and potentially resource-demanding map refinement, loop closing, and pose graph optimization.

The design of the frontend pipeline prioritizes local pose estimation accuracy over global consistency, focusing on delivering smooth trajectories without the bumps introduced by loop closure mechanisms or PGO (Pose Graph Optimization). To achieve this, it maintains a local odometry map consisting of the last N 6DOF camera poses (at keyframes) along with visible 3D landmarks and their observations. Besides the map, the frontend consists of the 2D module, responsible for feature selection, 2D feature tracking, and keyframe selection, and the 3D module, which performs pose estimation based on the local map, 2D information, and other data sources (e.g., IMU or depth measurements).

In contrast to the frontend, cuVSLAM backend focuses on global map and pose consistency. It processes frontend outputs and builds a globally consistent map that integrates camera poses, 2D observations, 3D landmarks, pose deltas, and visual features. The backend maintains global consistency in the map through asynchronous refinement using pose graph optimization and loop closing.

2.1. 2D module

cuVSLAM implements a set of algorithms operating on the 2D level, which include keypoint selection and feature extraction, keypoint tracking, and keyframe selection.

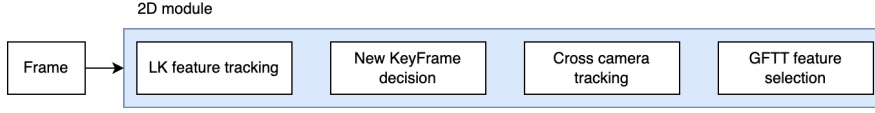


Figure 2: 2D module implements keyframe selection, feature selection and 2D tracking.

The pipeline begins with keypoint selection, which is designed to identify high-contrast features and ensure an approximately uniform distribution of keypoints across the image. The image is first divided into non-overlapping patches, forming an $N \times M$ grid. In each patch, the algorithm selects the top k keypoints based on the "Good Features to Track" measure (Shi and Tomasi (1993)), where k is calculated such that the total number of keypoints across the entire image exceeds a predefined threshold, K_I .

$$k > \left\lceil \frac{K_I}{N * M} \right\rceil \quad (1)$$

For 2D tracking, cuVSLAM implements a modified version of the Lucas-Kanade algorithm (Lucas and Kanade (1981), Bouguet (2000)) for feature tracking that: 1) performs tracking in a coarse-to-fine manner, continuously refining track positions at each image pyramid level, and 2) performs a normalized cross-correlation (NCC) check at each optimization step for each keypoint to filter out unreliable tracks.

If the number of successfully tracked keypoints falls below a threshold, the 2D module creates a new keyframe, which triggers local and global map updates and asynchronous refinement. In stereo and multicamera modes, cuVSLAM launches cross-camera feature tracking to obtain multi-view observations for subsequent landmark triangulation.

2.2. 3D module

When a keyframe is created, the 3D module collects multi-view observations from the 2D module and performs landmark triangulation. The created landmarks, along with their observations, are saved in the local map. After pose estimation, an asynchronous local sparse bundle adjustment (SBA) is initiated for refinement. Given the poses T_i , landmarks p_j , and 2D observations o_{ij} , SBA solves the following optimization task:

$$r_{ijk}^{repr} = \pi(T_k^{cb} T_i^{bw} p_j^w) - o_{j,k} \quad (2)$$

$$\hat{T}_{1:N}^{bw}, \hat{p}_{1:M}^w = \arg_{T_{1:N}^{bw}, p_{1:M}^w} \min \sum_{i \in [1, N]} \sum_{j \in [1, M]} \sum_{k \in [1, C]} \|\pi(T_k^{cb} T_i^{bw} p_j^w) - o_{j,k}\|_{\Sigma}^2 \quad (3)$$

where r^{repr} represents reprojection error, T_k^{cb} refers to the k -th camera-from-base transformation, T_i^{bw} denotes the base-from-world transformation, p^w is the 3D landmark in the world frame, and $o_{j,k}$ represents the observation of landmark j by the k -th camera.

Following the common approach, we use the Schur complement to solve for poses T_i first and solve for points p_j afterward. To enhance the efficiency of SBA further, we implement it in CUDA, which is particularly useful for edge devices and/or in multicamera setups. cuVSLAM supports mono, stereo, multicamera, and visual-inertial modes, each of which corresponds to a dedicated 3D solver.

2.2.1. Stereo

Stereo mode is the default mode in cuVSLAM. It utilizes PnP algorithm for pose estimation, that relies on o_j , 2D observation, and p_i , 3D landmarks, acquired from the local map.

$$\hat{T}^{bw} = \arg_{T^{bw}} \min \sum_{j \in [1, M]} \sum_{k \in [1, 2]} \|r_{jk}^{repr}\|_{\Sigma}^2 \quad (4)$$

On regular frames, we perform tracking only for the left camera for the tracks that are still active. We query the local map for the corresponding 3D landmarks and use them for pose estimation. When the number of successfully tracked keypoints falls below a threshold, a keyframe is created. After feature selection, we perform cross-camera (left-to-right) tracking to obtain landmark stereo observations and conduct point triangulation. Finally, we add the current camera pose, along with the created landmarks and their observations, into the local map and launch asynchronous SBA for refinement.

2.2.2. Multi-Stereo

When a robot operates in environments where it is likely to face a featureless surface from one direction, e.g., narrow corridors or elevators, it becomes vital to use multiple cameras for pose estimation.

cuVSLAM extends the approach introduced in 2.2.1 to a multicamera setup by treating an arbitrary multiple-camera configuration as a number of stereo pairs.

At startup, we build a Frustum Intersection Graph (FIG)—a directed graph (V, E) , where vertices V represent a set of optical sensors, and edges E connect cameras that share a common field of view. Edge direction describes the cross-camera tracking between adjacent cameras, i.e., if e_{ij} exists, cuVSLAM performs 2D tracking from camera c_i to c_j .

The FIG is built automatically at cuVSLAM startup. Provided with a list of camera extrinsics/intrinsics, cuVSLAM iterates over each pair of cameras and creates a new edge in the graph when cameras have overlapping fields of view (FoV). To detect this, cuVSLAM places a virtual plane in front of the first camera. It selects uniformly distributed pixels in the image I_1 , lifts them onto the plane, and backprojects them to the image I_2 . When the ratio of successfully projected points to the total number of sampled points exceeds a threshold, cuVSLAM detects the shared FoV and creates an edge.

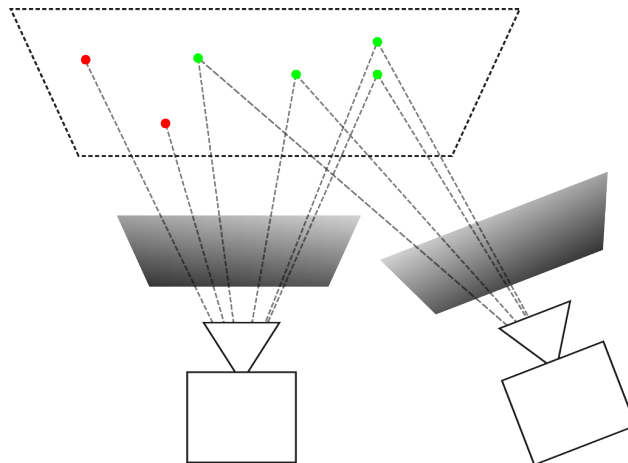


Figure 3: Randomly selected pixels on left picture are lifted on a virtual plane in front of the camera. Pixels that can be successfully projected onto second images are shown in green.

Cameras that correspond to the source of some edge are used for feature tracking/selection over time on each incoming frame. A keyframe is still treated as a global event, while feature selection happens independently

for each camera.

Let S_{curr} be a set of all currently observed points from all the cameras and S_{kf} is the set of points observed in the previous keyframe. Then if:

$$\frac{|S_{curr} \cap S_{kf}|}{|S_{kf}|} < T; \quad (5)$$

a keyframe is created and cross-camera tracking is done. Similar to stereo mode we then perform landmark triangulation and refine the map with SBA.

After 2D tracking both on regular frames and keyframes, we collect all the available observations along with the corresponding 3D landmarks for pose estimation.

$$\hat{T}^{bw} = \arg_{T^{bw}} \min \sum_{j \in [1, M]} \sum_{k \in [1, C]} \|r_{jk}^{repr}\|_{\Sigma}^2 \quad (6)$$

where r^{repr} denotes a reprojection error for j -th landmark observed from k -th camera in the rig [Barfoot \(2017\)](#).

Since observations from multiple cameras contribute to pose estimation, cuVSLAM requires images to be synchronized. This is a minor restriction, as many modern cameras provide hardware synchronization capabilities, such as Intel RealSense [Grunnet-Jepsen et al. \(2018\)](#).

2.2.3. Visual-Inertial

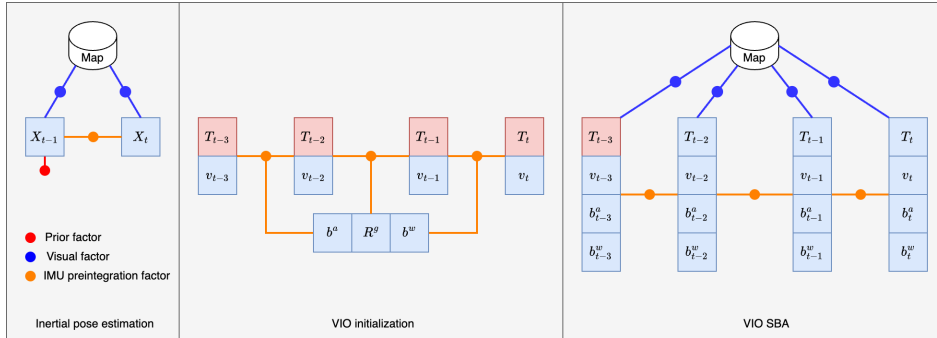


Figure 4: Factor graphs for VIO pipeline.

Visual-Inertial (VI) mode is inspired by [Forster et al. \(2017\)](#) and [Campos et al. \(2021\)](#). Following their approach cuVSLAM defines robot's state as a combination of 6 DoF pose, linear velocity, accelerometer and gyroscope biases forming a 15 DoF state vector $S = [T \in SE(3), v \in \mathbb{R}^3, b^a \in \mathbb{R}^3, b^w \in \mathbb{R}^3]$. Robot states along with IMU (r^{imu}) and visual (r^{repr}) factors are used to build a factor-graph for a list of crucial subproblems, which are:

- *Purely visual pose estimation* is used for the initialization of VI pipeline. It consists of the PnP and the asynchronous SBA as it was described in section 2.2.1 and needed to build a pose history for the subsequent gravity estimation.
- *Gravity estimation*. Gravity is a key parameter needed for the IMU preintegration and IMU-aided pose estimation. Assuming the poses predicted by the visual-only part are fixed, the algorithm estimates velocities v_i , accelerometer and gyroscope biases b^a , b^w and a rotation matrix R^g , s.t. $g = R^g[0, 0, 9.81]^T$.

$$R^g, \mathbf{b}, v_{0:k} = \operatorname{argmin} \left[\|b\|_{\Sigma_{prior}}^2 + \sum_{i=0}^{k-1} \|r^{imu}(S_i, S_{i+1})\|_{\Sigma_{IMU}}^2 \right] \quad (7)$$

- *Visual-inertial pose estimation* is used every frame. It constrains two consecutive robot states S_{i-1} and S_i with IMU and visual factors. In addition S_{i-1} is also constrained by the prior factor.

$$S_{i-1}, S_i = \underset{S}{\operatorname{argmin}} \left[\|r^{imu}(S_{i-1}, S_i)\|_{\Sigma_{IMU}}^2 + \sum_{j=0}^1 \|r^{repr}(S_{i-j})\|_{\Sigma_{vis}}^2 + \|r^{prior}(S_{i-1})\|_{\Sigma_p}^2 \right] \quad (8)$$

- *Visual-inertial sparse bundle adjustment* is used for local map refinement when IMU data along with gravity and bias estimations are available. Following prior works, we perform relinearization of the IMU factors based on the variable update norm or once per number of iterations.

$$S_{0:k} = \underset{S}{\operatorname{argmin}} \left[\sum_{i=1}^k \|r^{imu}(S_{i-1}, S_i)\|_{\Sigma_{IMU}}^2 + \sum_{i=0}^k \|r^{repr}(S_i)\|_{\Sigma_{vis}}^2 \right] \quad (9)$$

2.2.4. Mono-Depth

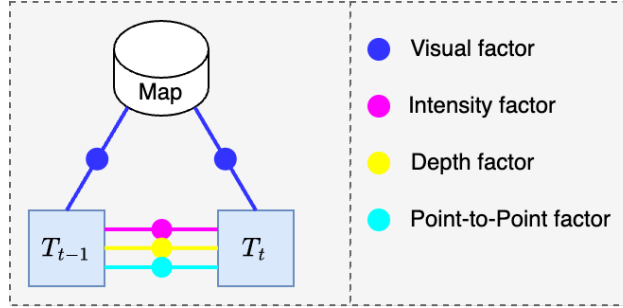


Figure 5: RGBD factor graph.

cuVSLAM supports mono RGBD-based dense frame-to-frame pose estimation. Following [Kerl et al. \(2013\)](#) it considers two consecutive intensity images $I_{1,2}$ along with pixel-aligned depth images $Z_{1,2}$ and estimates a relative 6 DoF transformation between corresponding frames.

It defines a list of factors, that constrain frame positions w.r.t each other:

- **Visual factor** used to constrain poses w.r.t the local map by means of reprojection error r^{repr} described earlier.
- **Dense intensity and depth factors** define constraints for each pixel location x , introducing the following error functions:

$$r^I = \begin{bmatrix} I_2(\tau(T_{21}, x)) - I_1 \\ I_1(\tau(T_{21}^{-1}, x)) - I_2 \end{bmatrix} \quad (10)$$

$$r^Z = \begin{bmatrix} Z_2(\tau(T_{21}, x)) - [T_{21}\pi^{-1}(x, Z_1(x))]_z \\ Z_1(\tau(T_{21}^{-1}, x)) - [T_{21}^{-1}\pi^{-1}(x, Z_2(x))]_z \end{bmatrix} \quad (11)$$

where T_{21} is the relative pose; $\tau(T, x)$ is a warping function, that lifts the pixel location x to 3D, applies transformation T and projects the point back to image plane; $[\cdot]_z$ returns Z coordinate of a point.

- **Point-to-point factor.** Provided with the 2D-2D matches $(x, y)_{1:N}$ obtained in 2D module, we define the point-to-point error:

$$r^p = \pi^{-1}(y, Z_2(y)) - T_{21}\pi^{-1}(x, Z_1(x)) \quad (12)$$

All together these factors form the combined optimization problem, which we solve using a Levenberg-Marquardt

solver implemented on GPU:

$$\hat{T}_{21} = \arg_{T_{21}} \min(\sum_{p \in Points} \|r^{repr}(p)\|_{\Sigma}^2 + \sum_{x \in Pixels} (\|r^I(x)\|^2 + \|r^Z(x)\|_{\sigma_z}^2) + \sum_{(x,y) \in Tracks} \|r^p(x,y)\|^2) \quad (13)$$

2.2.5. Mono

Mono camera mode shares the same common approach as 2D feature tracking, with subsequent point triangulation and pose estimation. A key difference is that triangulation is performed using observations obtained from different camera poses, which we estimate using the same PnP algorithm as described in 2.2.1, given the current observations of previously obtained landmarks.

For the first frame pair, when no 3D landmarks are available, cuVSLAM estimates the relative transformation through the fundamental matrix. Specifically, given a set of 2D tracks $(x, y)_{1:N}$, we estimate the fundamental matrix F using RANSAC. With the calibration matrix K , we then retrieve the up-to-scale relative pose.

The relative pose is subsequently used to triangulate the first set of landmarks and update the local map, followed by asynchronous SBA refinement.

2.3. Loop closing and global map refinement

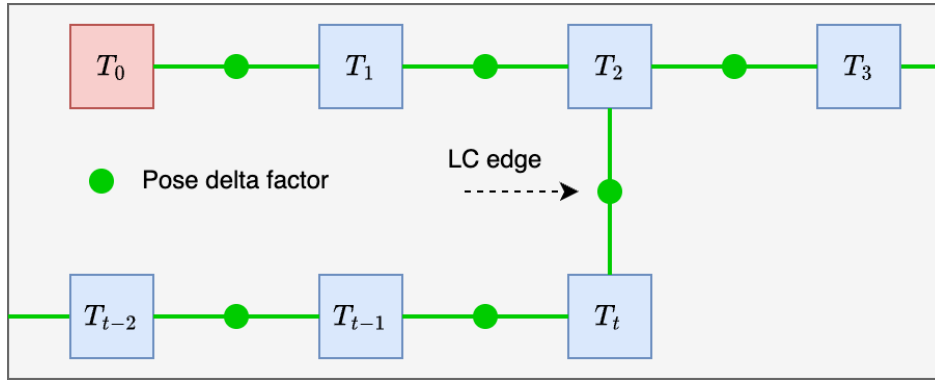


Figure 6: Factor graphs for VIO pipeline.

cuVSLAM loop closing and global map refinement module helps limit global drift by enforcing global consistency of the map. It consists of 6 DoF keyframe poses, landmarks and their observations, pose deltas, and sparse image features. Pose deltas are obtained through the integration of intra-keyframe frontend pose predictions. For image features, we use a list of 9×9 image patches taken from each level of the image pyramid.

We perform the following steps to detect loop closures and refine the map to enforce global consistency:

- **Integrate latest data.** When a new keyframe is created, cuVSLAM extracts visual features, integrates intra-keyframe pose predictions, collects currently visible landmarks along with their observations and updates the global map using an asynchronous data queue.
- **Query nearest neighbors.** After the map update, cuVSLAM performs a pose search of robot poses within a sphere of fixed radius. We use a kd-tree for fast and efficient spatial search.
- **Landmark selection.** After collecting all the landmarks related to the found poses, we: 1) filter them by geometric visibility, 2) track landmark visual features onto the currently observed image, and 3) filter out landmarks with unsuccessful tracking. Finally, when landmarks from multiple poses are observed, we split the landmarks into sets with respect to connected poses and pick the largest set.
- **Relative pose estimation.** At this step, we estimate a pose delta D between the pose from the map and the current robot's position. Let T^{mw} denote a pose in the map, connecting the *world* and *map* frames.

Then, after shifting landmarks into the *map* frame, we solve for the relative pose estimate:

$$\hat{T}^{bm} = \arg_{T^{bm}} \min \sum_{j \in [1, M]} \sum_{k \in [1, C]} \|\pi(T_k^{cb} T^{bm} T^{mw} p_j^w) - o_{j,k}\|_{\Sigma}^2 \quad (14)$$

- **Pose graph optimization.** Provided with the pose deltas between poses either by the frontend or the loop closure mechanism, cuVSLAM refines the map by minimizing the following sum across pose graph edges E :

$$T_{1:N} = \arg_{T_{1:N}} \min \sum_{i,j \in E} \|Log(D_{ij}^{-1} T_i^{-1} T_j)\|^2 \quad (15)$$

3. Experiments

This section demonstrates the capabilities of the cuVSLAM library in robotics applications across diverse real-world environments and camera configurations. We also compare our solution with established classical and deep learning libraries that provide camera pose estimation for long-distance trajectories.

3.1. System Performance and Hardware Utilization

We evaluated cuVSLAM performance through two complementary approaches: real-time execution on embedded hardware to measure resource utilization and single-frame processing time, and offline processing of warehouse environment recordings on workstation hardware. The test scenarios involved processing feature-rich images captured from either a wheeled robot navigating a warehouse environment or handheld camera movements. To ensure accurate measurements, all experiments were conducted on systems dedicated solely to cuVSLAM execution, without concurrent resource-intensive operations such as visualization, complex image processing, or data recording that could potentially skew the results.

Table 1 summarizes the key performance metrics, with comprehensive results provided in Appendix A.2. The left portion of Table 1 presents execution times for cuVSLAM visual tracking function, excluding image acquisition and post-processing overhead. These measurements were obtained using recorded color images at 768×480 resolution (with the exception of mono-depth mode at 640×480 resolution) on two distinct hardware configurations: a desktop workstation featuring an Intel i7-14700 CPU with NVIDIA RTX 4090 GPU, and an embedded Jetson Orin AGX 64GB single-board computer operating in MAXN power mode.

Table 1: cuVSLAM Performance Evaluation. Left: Per-call processing times measured on RTX 4090 (Desktop) and Jetson AGX Orin (64 GB) using datasets with image resolution 768×480 (except mono-depth mode at 640×480). Right: CPU and GPU utilization on Jetson AGX Orin during live operation with RealSense cameras at 640×480 resolution and 60 FPS (except stereo-inertial mode at 30 FPS).

Configuration	Track call time, ms		Jetson HW utilization	
	Desktop	Jetson	CPU %	GPU %
Mono	0.9	2.7	NA	NA
Mono-Depth	5.9	15.1	2.6	55.0
Stereo-Inertial	1.3	3.8	1.3	2.2
Stereo	0.4	1.8	5.5	1.7
Multicamera (2-stereo)	0.8	2.0	8.3	9.0
Multicamera (3-stereo)	1.4	2.3	8.3	11.0
Multicamera (4-stereo)	2.1	NA	NA	NA

The right portion of Table 1 details CPU and GPU utilization percentages for cuVSLAM visual odometry executed through ISAAC ROS 3.2 with RealSense D435/D455 stereo cameras. All live tests utilized cameras configured at 640×480 resolution and 60 FPS, except for Stereo-Inertial mode, which ran at 30 FPS with IMU data at 200 Hz. The reduced framerate was necessary to ensure valid IMU-based integration, providing 6-7 IMU measurements between each stereo image pair. To accurately isolate cuVSLAM hardware requirements, we

employed a controlled experimental methodology: we first established baseline system utilization with the RealSense camera in motion but without cuVSLAM processing, then repeated the similar camera movement pattern with cuVSLAM visual tracking active. Resource utilization metrics were sampled at 15 ms intervals for equal durations in both experiments. The net resource consumption attributable to cuVSLAM was calculated by subtracting baseline measurements from total utilization values and averaging the results. This methodology provides an accurate assessment of the computational overhead introduced by the library. Additional details on evaluation and an exploration of hardware utilization across different resolutions and modes on Jetson devices are provided in Appendix A.2.

3.2. Benchmarking

We evaluated cuVSLAM different operation modes using several publicly available datasets. The Mono-Depth mode was validated on the AR-table [Chen et al. \(2023\)](#), ICL-NUIM [Handa et al. \(2014\)](#) and TUM RGB-D [Sturm et al. \(2012\)](#) datasets. The Stereo mode was tested on the EuRoC [Burri et al. \(2016\)](#) and KITTI [Geiger et al. \(2013\)](#) datasets. The Stereo-Inertial mode was assessed using the EuRoC [Burri et al. \(2016\)](#) and TUM-VI [Schubert et al. \(2018\)](#) datasets. The Multi-Stereo mode was evaluated on simulated TartanAir V2 [Wang et al. \(2023\)](#) and TartanGround [Patel et al. \(2025\)](#) datasets and our proprietary R2B real-world dataset.

Table 2: Evaluation results for cuVSLAM Visual Odometry and SLAM across various operating modes

Mode	Dataset	Method	avgRTE, %	avgRE, deg	RMSE APE
Mono-Depth	AR table	ORB_SLAM3	-	-	-
		DPVO	4.42	1.65	0.77
		cuVSLAM Odom	0.34	3.59	0.09
		cuVSLAM SLAM	0.19	1.68	0.025
	ICL-Nuim	ORB_SLAM3	-	-	-
		DPVO	10.28	0.77	0.61
		cuVSLAM Odom	0.41	0.99	0.026
		cuVSLAM SLAM	0.44	0.97	0.026
	TUM RGB-D	ORB_SLAM3	0.50	2.98	0.067
		DPVO	13.56	1.98	0.80
		cuVSLAM Odom	1.35	5.52	0.11
		cuVSLAM SLAM	0.99	4.13	0.065
Stereo	EuroC*	ORB_SLAM3	0.21	1.41	0.068
		DPVO	0.21	0.96	0.10
		cuVSLAM Odom	0.29	1.96	0.13
		cuVSLAM SLAM	0.17	1.12	0.054
	Kitti	ORB_SLAM3	0.31	1.20	2.98
		DPVO	21.69	1.14	195.05
		cuVSLAM Odom	0.33	1.14	3.00
		cuVSLAM SLAM	0.27	0.93	1.98
Stereo-Inertial	EuroC	ORB_SLAM3	5.70	72.23	0.066
		DPVO	-	-	-
		cuVSLAM Odom	0.39	2.69	0.19
		cuVSLAM SLAM	0.29	2.27	0.13
	TUM-VI Room	ORB_SLAM3	2.17	1.37	0.077
		DPVO	-	-	-
		cuVSLAM Odom	0.20	3.85	0.18
		cuVSLAM SLAM	0.12	3.00	0.12

To quantify visual tracking accuracy, we employed standard metrics: Average Relative Translation (avgRTE) and Rotation (avgRE) Errors [Geiger et al. \(2013\)](#), and Absolute Pose Error (RMSE APE) with trajectory alignment and scale correction [Sturm et al. \(2012\)](#) using the EVO library [Grupp \(2017\)](#).

Table 2 presents comprehensive benchmarking results across popular datasets from various domains. For

comparative analysis, we include performance metrics for the classical computer vision-based ORB-SLAM3 and the deep learning-based DPVO alongside cuVSLAM. Each library was configured according to the dataset characteristics: ORB-SLAM3 and cuVSLAM operated in their corresponding specialized modes (monocular-depth, stereo, or stereo-inertial), while DPVO consistently used monocular mode across all evaluations, utilizing the front-left camera for stereo datasets. Since scale corrections were applied to final trajectories rather than successive pose estimations, translation results may not be meaningful for some datasets; therefore, relative rotation error should be considered the primary metric.

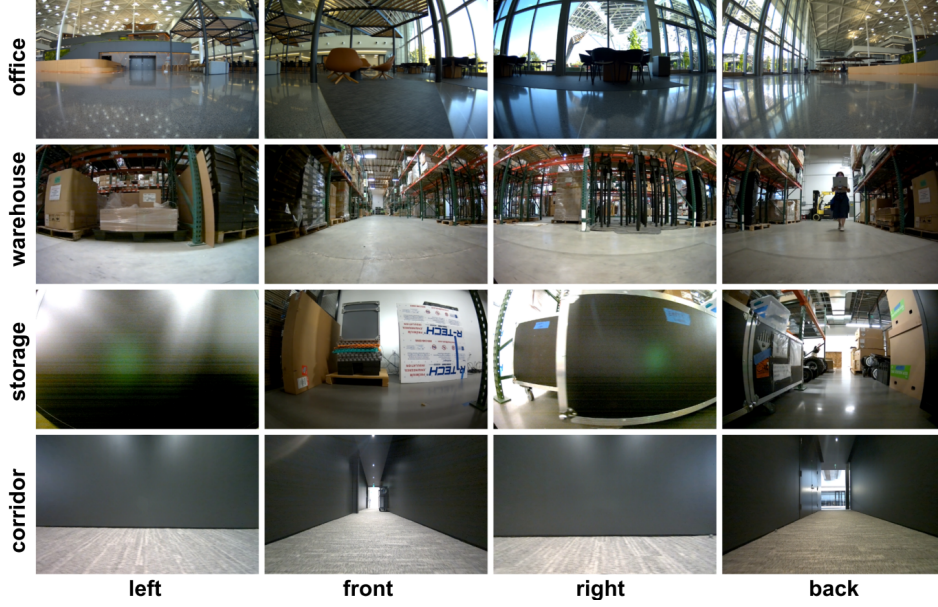


Figure 7: Sample camera views from the R2B dataset captured across diverse environments including large office spaces, industrial warehouses, and narrow corridors in both office and storage areas. The images show simultaneous captures from 4 stereo cameras (displaying only the left image from each stereo pair).

To ensure accurate and representative comparisons, we excluded clearly identified outlier and corrupted sequences. For instance, the EuRoC V203 sequence was included only in Stereo-Inertial evaluations, and only a subset of TUM RGB-D sequences were used (see Table 6). For TartanGround datasets, not all sequences provide the full complement of cameras or are available for download. Additionally, many sequences lack overlapping trajectories, preventing loop closure detection—a critical component for evaluating SLAM performance versus odometry. Consequently, we validated SLAM mode on selected subsets of TartanGround (see Table 9) and TartanAir V2 (see Tables 10 and 11) datasets.

While the new Tartan datasets provide free camera and quadruped robot movements in diverse simulated environments, rigorous validation of cuVSLAM multi-camera capabilities in real-world scenarios was required. Therefore, a proprietary Multi-Stereo R2B dataset was collected in office and warehouse environments using the Nova Carter wheeled robot equipped with four stereo cameras. The example views from the R2B dataset are shown in Fig. 7. This was our only available option for validating this cuVSLAM mode on real data, as publicly available real-world multi-camera datasets either lack hardware-synchronized cameras suitable for stereo pair arrangements [Carlevaris-Bianco et al. \(2015\)](#); [Nair et al. \(2024\)](#) or employ software synchronization that cannot ensure simultaneous image capture [Yin et al. \(2021\)](#); [Zhang \(2023\)](#).

Table 3 presents cuVSLAM results in Multi-Stereo Mode. Notably, results achieved on the real R2B dataset closely match those from similar domains in the TartanGround dataset, confirming the validity of both datasets and results. For TartanAir V2, we performed detailed validation only on the Hard dataset, which presents greater challenges due to fast six-degrees-of-freedom motion and higher translational and angular velocities.

Table 3: Evaluation results for cuVSLAM Multi-Stereo Visual Odometry and SLAM on multi-camera datasets

Dataset	Method	avgRTE, %	avgRE, deg	RMSE APE
R2B	cuVSLAM Odom	0.18	1.15	0.28
	cuVSLAM SLAM	0.11	0.70	0.18
TartanGround	cuVSLAM Odom*	0.54	0.95	0.14
	cuVSLAM Odom	0.21	0.48	0.09
	cuVSLAM SLAM	0.17	0.37	0.07
TartanAir V2 (Hard)	cuVSLAM Odom*	2.56	13.97	5.20
	cuVSLAM Odom	2.44	13.98	5.24
	cuVSLAM SLAM	2.26	12.76	4.99

Results for the Easy mode are comparable to those for TartanGround, with a detailed comparison available in Table 8. While TartanAir V2 results indicate room for improvement, they also demonstrate the importance of multi-camera mode for robust tracking in most environments, with some showing 2–4 \times improvement in multi-camera SLAM mode.

We anticipate that the recent growth in availability and adoption of synchronized multi-stereo camera systems from various vendors will encourage the creation of new public multi-camera datasets, facilitating further development, testing, and implementation of multi-camera SLAM systems in robotic applications.

4. Discussion

We advocate for the wider adoption of multi-camera visual tracking in robotics based on two principal advantages observed in our experiments: enhanced trajectory reliability in feature-poor environments when operating in odometry mode, and increased loop closure detection rates in SLAM mode.

4.1. Trajectory Reliability Under Visual Occlusion

Figure 8 demonstrates the system’s trajectory reliability through a practical robustness test. We equipped a Carter robot with 4 stereo cameras and subjected it to challenging visual conditions during continuous motion. Cameras were randomly occluded with opaque film for intervals of 20–60 seconds, with the constraint that at least one stereo pair remained unobstructed at a given moment.

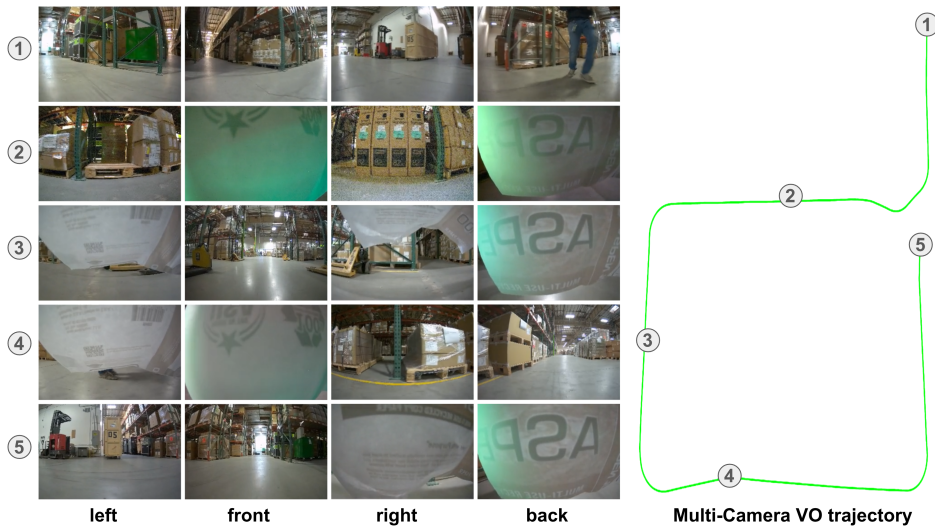


Figure 8: Occlusion resilience test using the Carter robot. cuVSLAM maintains continuous trajectory despite random camera occlusions. Numbered rows show instantaneous views from the robot’s 4 stereo cameras (left images only) at corresponding trajectory locations

Despite these severe visual constraints, the odometry trajectory maintained stability without exhibiting jumps or discontinuities, validating the system’s robustness to partial visual obstruction. This capability represents a significant advancement for visual tracking systems. While single-camera configurations can maintain tracking in feature-poor environments only briefly—typically relying on IMU or depth sensor fusion—our multi-camera approach preserves stable and reliable visual tracking over extended periods even with degraded visual input.

4.2. Enhanced Loop Closure Detection

The expanded collective field of view afforded by multiple cameras directly translates to increased loop closure detection rates. Figure 9 presents a comparative analysis of loop closure events between single-stereo and four-stereo camera configurations along identical trajectories. The multi-camera setup demonstrates a substantially higher frequency of successful loop closures, enabling more frequent pose graph optimization. This increased loop closure rate yields quantitative improvements in localization accuracy. As shown in Table 3, evaluation on the Multi-Stereo R2B dataset reveals approximately 40% improvement in SLAM accuracy metrics compared to pure odometry mode, underscoring the practical benefits of the multi-camera approach for robust localization.

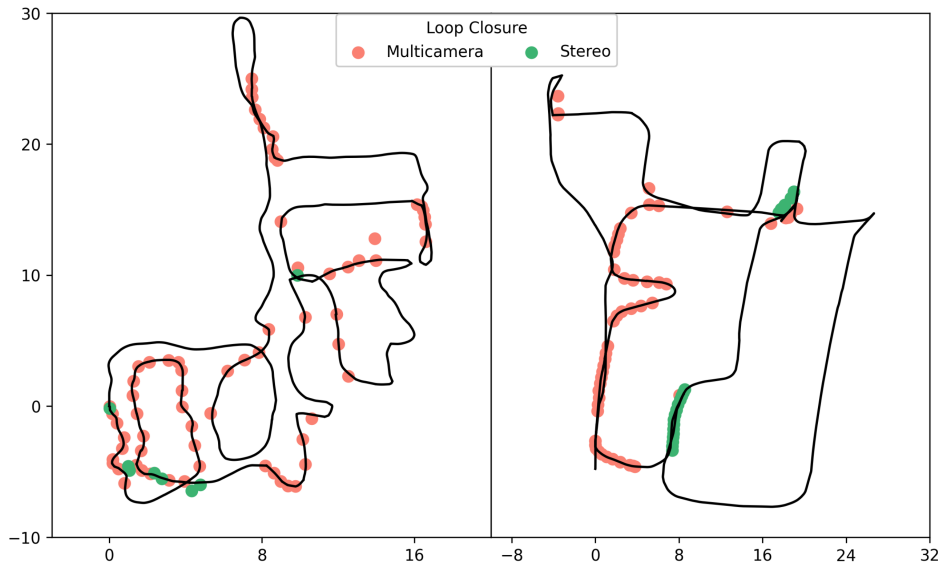


Figure 9: Comparison of loop closure detection events between single-camera and multi-camera (four stereo pairs) SLAM configurations on identical trajectories. The multi-camera setup demonstrates improved mapping consistency due to its wider cumulative field-of-view.

5. Conclusions

This technical report demonstrates the robust real-time performance of the cuVSLAM visual tracking library across diverse robotic platforms, including automotive vehicles, aerial drones, wheeled robots, and handheld camera systems. Our comprehensive evaluation encompasses both real-world deployments and synthetic datasets, validating the system’s capabilities under varied operational conditions.

The cuVSLAM library offers several key advantages that position it as a production-ready solution for modern robotics applications:

- **Accessibility and Integration:** The library is readily available through both ISAAC ROS¹ and Python² APIs, supporting deployment on both desktop and embedded NVIDIA platforms. This dual-API approach ensures flexibility for developers working across different software ecosystems.

¹https://github.com/NVIDIA-ISAAC-ROS/isaac_ros_visual_slam

²<https://github.com/NVlabs/PyCuVSLAM>

- **Computational Efficiency:** The system maintains low computational overhead while delivering high-accuracy localization, enabling seamless integration into complex robotic stacks such as NVIDIA Isaac Perceptor³, which incorporates NVBLOX [Millane et al. \(2024\)](#) for 3D reconstruction and Nav2 [Macenski et al. \(2020\)](#) for autonomous navigation.
- **Minimal Configuration Overhead:** Unlike many SLAM systems that require extensive parameter tuning for different scenarios, cuVSLAM provides robust out-of-the-box performance across diverse environments and sensor configurations, significantly reducing deployment time and complexity.

Looking forward, the demonstrated multi-camera capabilities and robust performance characteristics of cuVSLAM establish a strong foundation for next-generation autonomous systems that demand reliable visual localization in challenging real-world environments. The library's proven versatility across platforms and scenarios, combined with its efficient GPU-accelerated implementation, makes it a compelling choice for both research prototypes and production robotic systems.

³<https://developer.nvidia.com/isaac/perceptor>

References

- [1] Kitti visual odometry / slam evaluation 2012. URL https://www.cvlibs.net/datasets/kitti/eval_odometry.php. Accessed: 2025-06. 15
- [2] Tartanair: A python package for the tartanair-v2 dataset. URL <https://github.com/castacks/tartanairpy>. Accessed: 2025-06. 17
- [3] Timothy Barfoot. *State Estimation for Robotics*. 08 2017. ISBN 9781107159396. doi: 10.1017/9781316671528. 5
- [4] J. Y. Bouguet. Pyramidal implementation of the affine lucas kanade feature tracker description of the algorithm. *Microprocessor Research Labs*, 2000. URL https://robots.stanford.edu/cs223b04/algo_tracking.pdf. 3
- [5] Michael Burri, Janosch Nikolic, Pascal Gohl, Thomas Schneider, Joern Rehder, Sammy Omari, Markus W Achtelik, and Roland Siegwart. The euroc micro aerial vehicle datasets. *The International Journal of Robotics Research*, 35(10):1157–1163, 2016. doi: 10.1177/0278364915620033. 9
- [6] Carlos Campos, Richard Elvira, Juan J. Gomez Rodriguez, Jose M. M. Montiel, and Juan D. Tardos. Orbslam3: An accurate open-source library for visual, visual-inertial, and multimap slam. *IEEE Transactions on Robotics*, 37(6):1874–1890, December 2021. ISSN 1941-0468. doi: 10.1109/tro.2021.3075644. URL <http://dx.doi.org/10.1109/TR0.2021.3075644>. 5
- [7] Nicholas Carlevaris-Bianco, Arash K. Ushani, and Ryan M. Eustice. University of Michigan North Campus long-term vision and lidar dataset. *International Journal of Robotics Research*, 35(9):1023–1035, 2015. 10
- [8] Chuchu Chen, Patrick Geneva, Yuxiang Peng, Woosik Lee, and Guoquan Huang. Monocular visual-inertial odometry with planar regularities. In *2023 IEEE International Conference on Robotics and Automation (ICRA)*, pages 6224–6231, 2023. doi: 10.1109/ICRA48891.2023.10160620. 9, 16
- [9] Christian Forster, Luca Carlone, Frank Dellaert, and Davide Scaramuzza. On-manifold preintegration for real-time visual-inertial odometry. *IEEE Transactions on Robotics*, 33(1):1–21, February 2017. ISSN 1941-0468. doi: 10.1109/tro.2016.2597321. URL <http://dx.doi.org/10.1109/TR0.2016.2597321>. 5
- [10] Andreas Geiger, Philip Lenz, Christoph Stiller, and Raquel Urtasun. Vision meets robotics: The KITTI dataset. *The International Journal of Robotics Research*, 32(11):1231–1237, 2013. doi: 10.1177/0278364913491297. 9
- [11] Anders Grunnet-Jepsen, Paul Winer, Aki Takagi, John Sweetser, Kevin Zhao, Tri Khuong, Dan Nie, and John Woodfill. Using the intel® realsense™ d400 series depth cameras in multi-camera configurations. Technical report, Intel Corporation, 2018. URL <https://dev.intelrealsense.com/docs/multiple-depth-cameras-configuration>. Rev 1.2. 5
- [12] Michael Grupp. evo: Python package for the evaluation of odometry and slam. <https://github.com/MichaelGrupp/evo>, 2017. Accessed: 2025. 9
- [13] Ankur Handa, Thomas Whelan, John B. McDonald, and Andrew J. Davison. A benchmark for RGB-D visual odometry, 3D reconstruction and SLAM. In *2014 IEEE International Conference on Robotics and Automation (ICRA)*, pages 1524–1531, Hong Kong, China, May 2014. IEEE. doi: 10.1109/ICRA.2014.6907054. 9
- [14] Christian Kerl, Jürgen Sturm, and Daniel Cremers. Dense visual slam for rgb-d cameras. pages 2100–2106, 2013. doi: 10.1109/IROS.2013.6696650. 6

- [15] B. D. Lucas and T. Kanade. An iterative image registration technique with an application to stereo vision. *Proceedings of Imaging Understanding Workshop*, 1981. URL https://www.ri.cmu.edu/pub_files/pub3/lucas_bruce_d_1981_1/lucas_bruce_d_1981_1.pdf. 3
- [16] Steven Macenski, Francisco Martin, Ruffin White, and Juan Ginés Clavero. The marathon 2: A navigation system. In *2020 IEEE/RSJ International Conference on Intelligent Robots and Systems (IROS)*, pages 2718–2725. IEEE, 2020. 13
- [17] Alexander Millane, Helen Oleynikova, Emilie Wirbel, Remo Steiner, Vikram Ramasamy, David Tingdahl, and Roland Siegwart. nvblox: Gpu-accelerated incremental signed distance field mapping. 2024. URL <https://arxiv.org/abs/2311.00626>. 13
- [18] Ashish Devadas Nair, Julien Kindle, Plamen Levchev, and Davide Scaramuzza. Hilti slam challenge 2023: Benchmarking single + multi-session slam across sensor constellations in construction, 2024. URL <https://arxiv.org/abs/2404.09765>. 10
- [19] Manthan Patel, Fan Yang, Yuheng Qiu, Cesar Cadena, Sebastian Scherer, Marco Hutter, and Wenshan Wang. Tartanground: A large-scale dataset for ground robot perception and navigation, 2025. URL <https://arxiv.org/abs/2505.10696>. 9, 17
- [20] David Schubert, Thore Goll, Nikolaus Demmel, Vladyslav Usenko, Jörg Stückler, and Daniel Cremers. The TUM VI benchmark for evaluating visual-inertial odometry. *CoRR*, abs/1804.06120, 2018. URL <http://arxiv.org/abs/1804.06120>. 9, 16
- [21] Jianbo Shi and Carlo Tomasi. Good features to track. *1994 Proceedings of IEEE Conference on Computer Vision and Pattern Recognition*, 37(6), December 1993. ISSN 1063-6919. doi: 10.1109/CVPR.1994.323794. URL <https://ieeexplore.ieee.org/document/323794>. 3
- [22] Jürgen Sturm, Nikolas Engelhard, Felix Endres, Wolfram Burgard, and Daniel Cremers. A benchmark for the evaluation of rgb-d slam systems. In *2012 IEEE/RSJ International Conference on Intelligent Robots and Systems (IROS)*, pages 573–580. IEEE, Oct 2012. doi: 10.1109/IROS.2012.6385773. 9
- [23] Wenshan Wang, Yaoyu Hu, Yuheng Qiu, Shihao Shen, and Yorai Shaoul. Tartanair-v2 dataset, 2023. URL <https://tartanair.org>. Accessed: 2025-06. 9, 17
- [24] Jie Yin, Ang Li, Tao Li, Wenxian Yu, and Danping Zou. M2dgr: A multi-sensor and multi-scenario slam dataset for ground robots. *IEEE Robotics and Automation Letters*, 7(2):2266–2273, 2021. 10
- [25] Chaitanya; Zhang Christina; Hong Raymond; Kalyani Pranav; Kalyanaraman Lochana; Gamare Arsh; Bagad Arnav; Esteve Maria; Biswas Joydeep Zhang, Arthur; Eranki. Ut campus object dataset (coda), 2023. URL <https://doi.org/10.18738/T8/BBOQMV>. 10

A. Appendix

A.1. Appendix A. Detailed Description of Dataset Validation

A.1.1. KITTI Dataset

We evaluated our method on sequences 0-10 of the KITTI dataset, for which ground truth trajectories are available. For comparison with the conventional KITTI leaderboard (1), Figure 10 presents relative translation (avgRTE) and rotation (avgRE) errors calculated on trajectory segments of lengths 100, 200, 300, 400, 500, 600, 700, and 800 meters. In contrast Table 2 presents results calculated without trajectory segmentation to maintain metric comparability across different datasets.

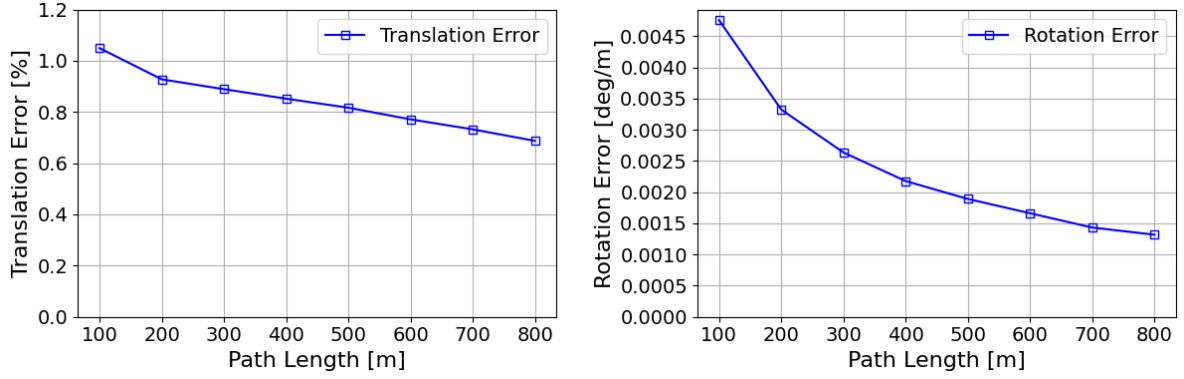


Figure 10: cuVSLAM evaluation results on KITTI odometry benchmark sequences 00-10. Translation and rotation errors are calculated on segments of 100-800m following the KITTI public leaderboard methodology, averaged metrics: **Translation: 0.85%, Rotation: 0.0025 [deg/m]**.

A.1.2. TUM-VI Room Dataset

To validate the stereo-inertial tracking mode on real hardware under aggressive camera motions, we evaluated cuVSLAM on the Room sequences of the TUM-VI dataset (20). These sequences were selected because they provide complete ground truth trajectories. We used undistorted images with a resolution of 512x512 pixels and applied a 50-pixel mask along each frame edge to mitigate significant fisheye lens distortion, which negatively affects tracking performance. To facilitate comparison with other visual tracking methods, we followed the evaluation protocol described in the original TUM-VI paper (20), computing the average RMSE of the Relative Pose Error (RPE) in meters/degrees over 1-second segments. Detailed results are provided in Table 4.

Table 4: cuVSLAM Stereo Inertial tracking validation results on TUM-VI Room dataset RMSE RPE (m / deg) on 1 second segments

Sequence	ODOM	SLAM
room1	0.023 / 0.89	0.025 / 0.90
room2	0.048 / 2.28	0.048 / 2.29
room3	0.047 / 1.93	0.048 / 1.95
room4	0.015 / 0.54	0.015 / 0.55
room5	0.019 / 0.56	0.021 / 0.57
room6	0.021 / 0.57	0.021 / 0.58

A.1.3. AR-table Dataset

This dataset contains sequences captured using an Intel RealSense D455 depth camera, providing image and depth data at a resolution of 848x480 pixels. The enhanced image and depth quality allows achieving performance on this real-world camera close to that obtained on the ideal simulated ICL-NUIM dataset, as shown in Table 2.

However, consistent gaps in depth values were observed along the sides and bottom edges of the depth images. To mitigate this issue, we applied static masking of 24 pixels on each side and 10 pixels at the bottom. Additionally, several prolonged depth-image dropouts (lasting more than one second) occurred in sequences 3, 4, 5, and 8. To address these interruptions, we segmented the affected sequences into continuous portions, executed tracking independently on each segment, and subsequently merged the results.

To facilitate comparison with other visual tracking methods, we followed the evaluation methodology described in the original AR-table dataset paper (8). Specifically, we computed Absolute Trajectory Error (ATE), reporting translation errors in centimeters and rotation errors in degrees. The obtained results are summarized in Table 5.

Table 5: cuVSLAM Mono-Depth Odometry and SLAM validation results on AR table dataset ATE (degree / cm)

Mode	table_01	table_02	table_03	table_04	table_05	table_06	table_07	table_08
ODOM	3.77 / 2.03	9.36 / 5.41	6.09 / 2.28	3.13 / 2.21	2.27 / 1.97	3.43 / 3.39	18.5 / 6.17	13.2 / 8.18
SLAM	2.98 / 1.76	2.23 / 1.77	2.11 / 0.87	2.12 / 1.64	1.24 / 1.22	1.93 / 1.23	8.88 / 3.82	4.83 / 3.69

A.1.4. TUM RGB-D Dataset

To validate the Mono-Depth mode on this dataset, a subset of 10 sequences from the Freiburg3 collection was used. These sequences were selected as they provide rectified images, which are required by cuVSLAM Mono-Depth mode. Minimal preprocessing was performed, consisting only of depth-image pair synchronization without further image or depth processing. The complete list of evaluated sequences is provided in Table 6.

Table 6: Results of cuVSLAM Mono-Depth Odometry and SLAM evaluation on TUM RGB-D dataset

Sequence	Mode	avgRTE	avgRE	RMSE APE
large cabinet validation	ODOM	1.74	2.08	0.12
	SLAM	1.53	1.60	0.11
long office household	ODOM	1.27	7.89	0.20
	SLAM	0.96	5.94	0.06
nostructure texture far	ODOM	1.29	1.66	0.07
	SLAM	1.44	1.63	0.06
nostructure texture near withloop	ODOM	1.23	4.62	0.10
	SLAM	1.25	4.71	0.04
sitting halfsphere	ODOM	2.07	3.67	0.12
	SLAM	0.61	1.42	0.05
sitting xyz	ODOM	1.03	1.21	0.05
	SLAM	0.65	0.86	0.03
sitting xyz validation	ODOM	0.90	1.42	0.05
	SLAM	0.44	0.67	0.03
structure texture far	ODOM	1.11	1.46	0.04
	SLAM	0.55	0.69	0.02
structure texture near	ODOM	1.45	2.15	0.03
	SLAM	1.45	2.09	0.03
teddy	ODOM	1.38	29.04	0.31
	SLAM	1.04	21.70	0.22

A.1.5. TartanGround and TartanAir V2

Odometry Mode. We validated cuVSLAM using 216 sequences from TartanGround (19) and 539 sequences from TartanAir V2 (23) Hard datasets. Complete sequence lists are provided in Tables 7 and 10, respectively. All results were obtained using a four stereo-camera configuration (front, back, left, and right) with 640×640 undistorted images. While the TartanAir V2 dataset supports two additional cameras (top and bottom), their inclusion yielded minimal metric improvement (less than 5%). For the TartanGround dataset, we observed slight performance degradation when using these additional cameras, attributed to meaningless feature selection from sky regions and repetitive floor textures in planar robot navigation areas.

To facilitate comparison with other visual tracking libraries, we computed additional metrics—relative translation (t_{rel}) and rotation (r_{rel}) per frame—using scripts from the official TartanAir GitHub repository (2). Since not all environments from the original TartanGround paper were available, we present environment-averaged results in Table 7 to enable future comparative studies.

TartanAir V2 Easy sequences were excluded from our analysis as they present minimal challenge for cuVSLAM, yielding consistently high tracking quality similar to the TartanGround dataset. To support this decision, Table 8

Table 7: Odometry evaluation results for cuVSLAM Multi-Stereo configuration (4 stereo cameras) on TartanGround dataset. Values represent averages computed per environment.

Environment	Sequences	avgRTE	avgRE	RMSE APE	t_{rel}	r_{rel}
Downtown	P0-P17	0.30	0.41	0.11	0.0019	0.00013
ForestEnv	P0-P22	0.45	0.72	0.19	0.0024	0.00036
Gascola	P0-P21	0.24	0.46	0.09	0.0012	0.00018
GreatMarsh	P1-P19, P21-P29	2.34	4.21	0.45	0.0037	0.00126
ModernCityDowntown	P1-P10	0.19	0.39	0.08	0.0012	0.00014
ModularNeighborhood	P0-P29	0.42	0.65	0.12	0.0014	0.00016
NordicHarbor	P0-P27	0.23	0.41	0.06	0.0010	0.00015
OldTownFall	P0-P7	0.15	0.34	0.04	0.0011	0.00013
OldTownSummer	P0-P7	0.15	0.34	0.05	0.0011	0.00013
SeasonalForestAutumn	P0-P19	0.27	0.42	0.11	0.0017	0.00022
SeasonalForestSpring	P0-P19	0.23	0.49	0.12	0.0016	0.00024
SeasonalForestWinter	P0-P21	0.27	0.51	0.08	0.0011	0.00018
Average		0.54	0.95	0.14	0.0017	0.00032

presents a comparison of averaged four-stereo-camera odometry results between Easy and Hard subsets of TartanAir V2, with example trajectory estimates shown in Figure 11.

Table 8: Comparative odometry evaluation of cuVSLAM Multi-Stereo (4 stereo cameras) on TartanAir V2 Easy and Hard sequences. Results show average performance metrics for selected environments.

Environment	Difficulty	avgRTE	avgRE	RMSE APE
AbandonedCable	easy	0.05	0.56	0.26
	hard	1.93	14.5	8.65
AbandonedFactory2	easy	0.02	0.13	0.02
	hard	0.27	1.41	0.34
CoalMine	easy	0.03	0.16	0.02
	hard	0.37	1.25	0.56
GothicIsland	easy	0.08	0.58	0.17
	hard	1.73	13.44	4.48
Hospital	easy	0.04	0.60	0.06
	hard	1.50	16.17	3.25
JapaneseAlley	easy	0.06	0.34	0.06
	hard	0.97	5.45	0.50
OldBrickHouseDay	easy	0.06	0.54	0.04
	hard	1.74	11.15	1.48

SLAM Mode. To evaluate the impact of SLAM mode on trajectory estimation, we analyzed only sequences containing loop closures. This resulted in a subset of 32 sequences for TartanGround and 506 sequences for TartanAir V2 Hard. Complete tracking results are provided in Tables 9 and 10, with all results averaged across environments.

For the TartanAir V2 dataset, most environments utilized all available sequences. Sequences excluded from SLAM validation are marked with an asterisk (P*), while their corresponding visual odometry results are labeled ODOM*, indicating performance metrics computed across all available sequences for those specific environments, including the excluded sequences.

A.1.6. Mutli-Stereo R2B Dataset

The Multi-Stereo R2B dataset was acquired using a wheeled Carter robot platform equipped with four stereo Hawk cameras, each capturing RGB images at a resolution of 1920×1200 pixels and 30 frames per second. The stereo camera pairs are hardware-synchronized to ensure temporal coherence, with synchronization precision

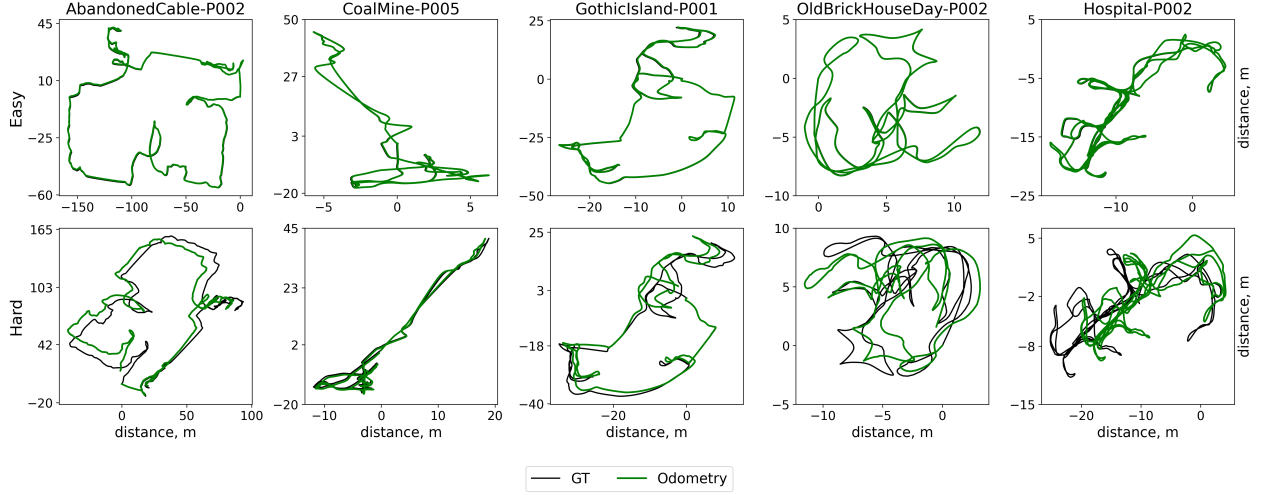


Figure 11: Example trajectories predicted by cuVSLAM (4 Multi-Stereo Odometry) on TartanAir V2 (Easy and Hard). Black lines represent ground truth, green lines represent odometry predictions. Columns correspond to the same environment and sequence label at different difficulties.

maintained within 0.1 ms for each 8-image batch. Data integrity validation confirmed minimal frame loss across all recordings, with the maximum batch loss rate remaining below 0.04%. Figure 12 illustrates the complete set of recorded trajectories, along with corresponding trajectory lengths and synchronized image batch counts for each sequence.

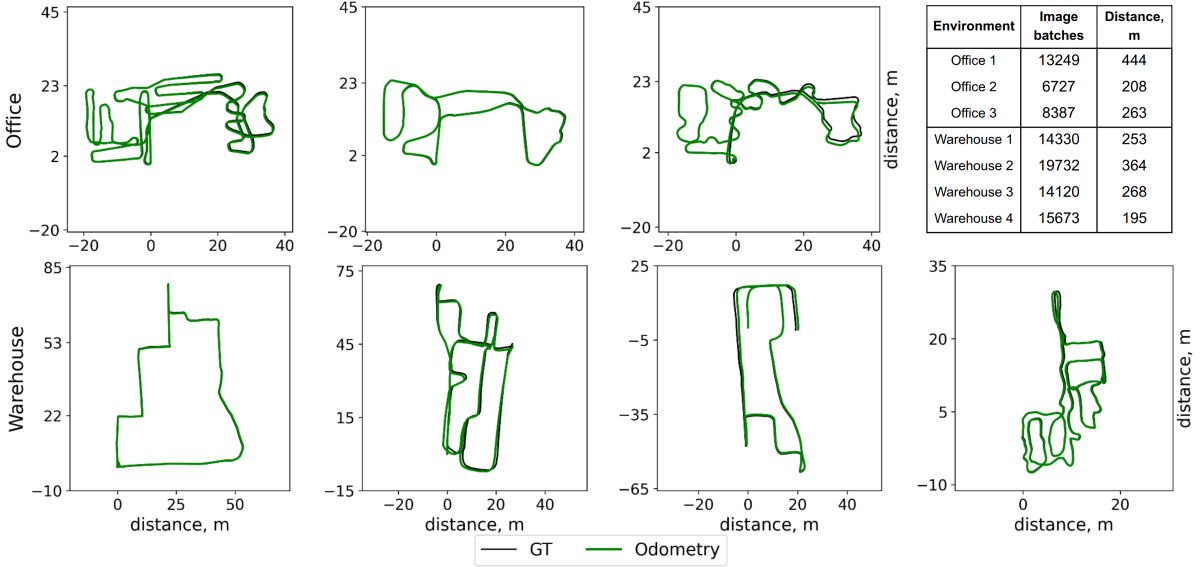


Figure 12: Trajectories predicted by cuVSLAM (4 Multi-Stereo Odometry) on the proprietary R2B wheeled robot dataset. Black lines represent ground truth; green lines represent odometry predictions. Attached table lists trajectory distances, number of 8-image batches, and trajectory index for environments (left to right).

A.2. Appendix B: Hardware Scalability on Embedded Platforms

This appendix presents an analysis of hardware utilization and visual tracking performance for cuVSLAM on embedded platforms, comparing Multi-Stereo and Mono-Depth modes as representative examples of sparse and dense feature-based approaches, respectively.

Experimental Setup. The primary hardware configuration consisted of an NVIDIA Jetson Orin AGX operating

in MAXN mode with 3 Intel RealSense D435 stereo cameras connected via USB and hardware-synchronized. Different resolutions were obtained directly from the cameras by modifying their configuration during the initialization step of each experiment. For Full HD resolution testing, we employed a set of 3 RGB Hawk stereo cameras connected via FAKRA2 connectors with hardware synchronization. All experiments were conducted in real-time with live camera feeds connected directly to the Jetson boards, and cuVSLAM calculations were performed on the same board in real-time. The system operated in Performance mode, utilizing the Isaac ROS (ROS2) stack for image acquisition and Multi-Stereo visual tracking, while the Python stack was employed for Mono-Depth visual tracking and processing.

Methodology. Resource utilization was measured through a two-phase experimental protocol designed to isolate the computational overhead of cuVSLAM. In the first phase, system utilization was logged while receiving frames from freely moving cameras without invoking visual tracking, establishing a baseline measurement. In the second phase, the identical setup was used with cuVSLAM visual tracking enabled. CPU and GPU utilization metrics were sampled at 15ms intervals, and the time spent on cuVSLAM frame processing was logged for each frame and subsequently averaged. The net computational resource utilization of cuVSLAM was calculated by subtracting the baseline measurements from the active tracking measurements.

Jetson Orin AGX Performance. Figure 13 illustrates the significant computational efficiency advantage of the sparse feature-based approach for tracking, demonstrating 3-7 \times faster processing times for 6-image batches compared to single image-depth pairs. The phenomenon where the 3-stereo camera visual tracking in Full HD configuration exhibited lower hardware utilization than HD configuration is attributed to differences in the camera field-of-view, with Hawk cameras provided $121.5^\circ \times 73.5^\circ$ FOV in FHD mode versus RealSense D435 cameras provided $87^\circ \times 58^\circ$ FOV in HD mode. The wider field-of-view affects the lifetime of keypoints as described in Section 2.1, triggering more frequent keyframe creation and consequently invoking computationally intensive operations including 3D landmark triangulation and sparse bundle adjustment, as detailed in Sections 2.1 and 2.2.

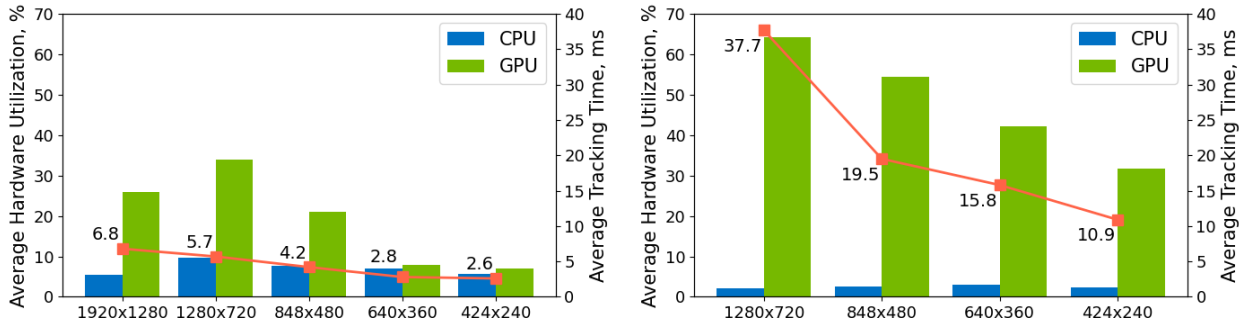


Figure 13: cuVSLAM realtime network hardware utilization and callback time per input image on Jetson AGX Orin as a function of resolution for 3-Stereo Camera Visual Odometry (left) and Mono-Depth Visual Odometry (right) at 30 FPS. For further details, refer to Appendix A.2

For Mono-Depth mode, the average callback time for 720p resolution reached 37.7ms, which exceeds the 33.3ms frame interval required for 30 FPS operation. This timing constraint indicates GPU overload on the Orin AGX platform in this configuration, and according to our measurements, resulted in the system skipping approximately half of the incoming frames. Consequently, for HD resolution applications, we recommend either reducing the frame rate to 15 FPS or decreasing the resolution to VGA, as our experiments revealed no significant difference in cuVSLAM visual tracking quality between VGA and HD resolutions.

Jetson Orin Nano Performance. To evaluate the feasibility of deploying cuVSLAM on entry-level hardware, we conducted experiments replacing the Jetson Orin AGX with a Jetson Orin Nano Super operating in 25W mode and utilizing exclusively the Python stack. The experiments explore possibility of using multi-stereo

odometry mode for 640x360 resolution and 30 FPS followed the methodology described above with free camera movement.

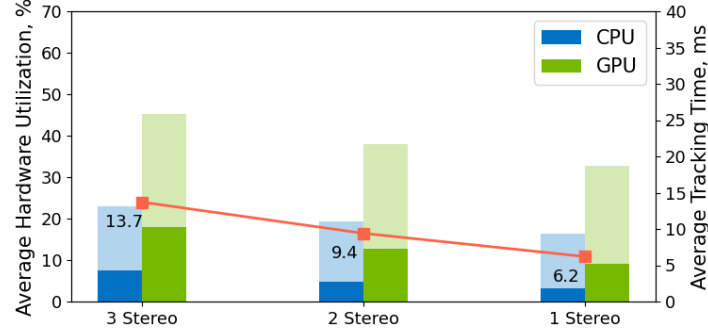


Figure 14: Hardware utilization and callback time on Jetson Orin Nano for Multi-Stereo Visual Odometry using RealSense cameras at 640×360 resolution and 30 FPS. Results are presented for varying numbers of cameras, showing total utilization (faded color bars) and net cuVSLAM utilization (normal color bars).

The results of average net cuVSLAM resource utilization, total system load, and average processing time are presented in Figure 14. The findings demonstrate substantial resource headroom, enabling the use of higher frame rates for configurations with one or 2 stereo cameras. For Mono-Depth processing at 30 FPS, stable operation was achieved only at the minimum resolution of 424×240 pixels. Although the average GPU load remained below 40%, the observed average cuVSLAM call time of 31ms approached the critical 33ms frame interval at 30 FPS. When combined with additional operations in the image acquisition loop, this resulted in exceeding the frame interval and consequently dropping approximately 30% of incoming frames.

It is important to note that for scenarios involving ground robots, the observed computational load will be lower than our free-movement test scenarios due to the reduced number of keyframes generated during predominantly inertial movements. However, for systems involving freely moving cameras with rapid scene changes, such as handheld cameras or unmanned aerial vehicles, we recommend increasing frame rates to 60 FPS when using RealSense cameras to ensure robust tracking performance. The selection of appropriate resolution and frame rate parameters should be carefully balanced based on the available computational resources and specific application requirements.

Table 9: Comparative evaluation of odometry and SLAM performance for cuVSLAM Multi-Stereo (4 stereo cameras) on the TartanGround dataset. To assess the impact of SLAM mode, a subset of sequences containing looped trajectories with observable loop closures was selected. Reported values are averages computed per environment.

Environment	Sequences	Mode	avgRTE	avgRE	RMSE APE
Downtown	P7	ODOM	0.35	0.59	0.09
		SLAM	0.25	0.41	0.09
ForestEnv	P1, P14, P17, P21	ODOM	0.42	0.78	0.16
		SLAM	0.38	0.61	0.17
Gascola	P0, P3-P6, P9	ODOM	0.17	0.41	0.08
		SLAM	0.13	0.31	0.06
ModernCityDowntown	P2, P5-P7	ODOM	0.17	0.32	0.08
		SLAM	0.12	0.24	0.06
ModularNeighborhood	P12, P20	ODOM	0.42	1.17	0.14
		SLAM	0.35	1.02	0.05
NordicHarbor	P1, P11, P17-P19 P23, P27	ODOM	0.17	0.41	0.08
		SLAM	0.10	0.26	0.04
OldTownFall	P2	ODOM	0.07	0.31	0.05
		SLAM	0.12	0.26	0.06
OldTownSummer	P2-P4	ODOM	0.09	0.29	0.06
		SLAM	0.06	0.25	0.03
SeasonalForestAutumn	P5, P8, P17	ODOM	0.20	0.32	0.07
		SLAM	0.19	0.33	0.07
SeasonalForestSpring	P9	ODOM	0.15	0.49	0.05
		SLAM	0.11	0.39	0.02
Average		ODOM	0.21	0.48	0.088
		SLAM	0.17	0.37	0.065

Table 10: TartanAir V2 Hard cuVSLAM evaluation results (Envs 1–35, see Appendix A.1.5 for details)

	Env	Seq	Mode	RTE	RRE	APE
1	Abandoned-Cable	P0-P7	ODOM SLAM	1.90 1.54	13.77 11.47	8.97 7.15
2	Abandoned-Factory	P1-P6 P8-P9	ODOM SLAM	1.07 0.77	4.89 3.70	1.06 0.95
3	Abandoned-Factory2	P0-P5	ODOM SLAM	0.27 0.19	1.41 0.84	0.34 0.24
4	Abandoned-School	P0-P9	ODOM SLAM	3.59 3.31	33.78 31.42	5.41 5.12
5	American-Diner	P0, P2* P3-P4	ODOM* ODOM SLAM	5.53 5.21 4.98	13.27 11.12 10.94	1.25 1.05 0.93
6	Amusement-Park	P0, P1* P2-P3, P4* P5-P7	ODOM* ODOM SLAM	1.15 1.36 1.36	3.74 5.15 5.49	1.53 1.71 1.71
7	Ancient-Towns	P0-P6	ODOM SLAM	2.86 2.50	10.98 8.93	2.52 2.23
8	Antiquity3D	P1-P5, P6* P7, P8*, P9	ODOM* ODOM SLAM	2.30 1.95 1.84	17.90 16.53 15.23	4.05 3.69 3.55
9	Apocalyptic	P0-P4	ODOM SLAM	0.92 0.66	4.25 2.81	1.25 0.98
10	ArchVizTiny-HouseDay	P0, P1* P2-P3, P4* P5-P6	ODOM* ODOM SLAM	3.75 2.69 2.44	4.02 3.48 3.14	0.37 0.27 0.25
11	ArchVizTiny-HouseNight	P0*, P1 P5, P6* P2-P4*	ODOM* ODOM SLAM	5.37 4.19 4.15	6.23 5.64 5.91	0.47 0.39 0.36
12	Brushify-Moon	P1-P5	ODOM SLAM	5.64 6.23	40.15 41.28	44.55 45.50
13	CarWelding	P0-P8	ODOM SLAM	1.14 0.94	5.74 4.51	1.34 1.27
14	Castle-Fortress	P0-P11	ODOM SLAM	0.93 0.90	7.33 6.41	2.65 2.50
15	CoalMine	P0-P5	ODOM SLAM	0.34 0.20	1.42 0.67	0.51 0.38
16	Construct-Site	P1, P3* P5* P6-P11	ODOM* ODOM SLAM	2.80 2.90 2.80	8.81 9.23 8.74	3.15 3.31 3.14
17	Country-House	P0-P5	ODOM SLAM	0.87 0.16	2.69 0.62	0.20 0.05
18	CyberPunk-Downtown	P0-P6	ODOM SLAM	1.19 1.27	7.27 8.22	4.01 3.98
19	Cyberpunk	P0-P7	ODOM SLAM	1.13 1.13	4.65 5.43	3.38 4.23
20	Desert-GasStation	P0-P4	ODOM SLAM	2.44 2.31	7.11 6.78	2.53 2.43
21	Downtown	P0-P8	ODOM SLAM	1.20 1.21	5.66 5.52	3.59 3.35
22	Factory-Weather	P1-P7, P8* P9-P12	ODOM* ODOM SLAM	6.23 6.31 6.17	39.06 40.09 37.40	22.37 22.64 22.22
23	Fantasy	P0-P6	ODOM SLAM	1.01 1.01	4.16 4.70	1.45 1.87
24	ForestEnv	P0, P2-P5 P7, P9 P10*, P11	ODOM* ODOM SLAM	3.67 3.55 3.62	21.93 21.75 23.64	13.76 14.42 15.47
25	Gascola	P0-P9	ODOM SLAM	2.36 2.49	14.83 14.56	5.47 6.13
26	Gothic-Island	P0-P10	ODOM SLAM	1.68 1.44	13.19 11.60	4.00 3.54
27	HQWestern-Saloon	P0-P7	ODOM SLAM	2.67 1.96	16.93 8.81	2.01 1.60
28	HongKong	P0, P1* P2-P4	ODOM* ODOM SLAM	5.26 4.81 4.75	18.85 18.85 17.78	5.02 3.99 3.89
29	Hospital	P0-P10	ODOM SLAM	1.50 1.30	16.17 14.85	3.25 2.93
30	House	P0-P7	ODOM SLAM	1.47 0.98	9.80 6.43	0.47 0.26
31	Industrial-Hangar	P0-P6	ODOM SLAM	3.43 3.48	19.61 19.86	8.21 8.03
32	Japanese-Alley	P0-P6	ODOM SLAM	0.94 0.34	5.27 1.87	0.48 0.39
33	Japanese-City	P0-P10	ODOM SLAM	1.81 1.74	7.89 7.80	2.08 2.03
34	MiddleEast	P0-P10	ODOM SLAM	2.96 2.65	13.18 11.34	2.64 2.47
35	Mod-UrbanCity	P0-P11	ODOM SLAM	3.65 3.70	23.51 23.22	5.74 5.60

Table 11: TartanAir V2 Hard cuVSLAM evaluation results (Envs 36–71, see Appendix A.1.5 for details)

	Env	Seq	Mode	RTE	RRE	APE
36	ModernCity-Downtown	P0-P8	ODOM SLAM	2.34 2.08	11.70 11.34	4.01 3.60
37	Modular-Neighborhood	P0-P10	ODOM SLAM	4.14 3.60	22.48 21.04	17.10 13.85
38	ModularNeighborhoodIntExt	P1-P5 P7-P8	ODOM SLAM	2.64 2.62	15.80 13.93	4.74 5.13
39	NordicHarbor	P0-P7	ODOM SLAM	2.07 1.97	14.37 15.04	6.04 5.77
40	Ocean	P1-P3 P4* P5-P7	ODOM* ODOM SLAM	1.76 1.65 1.47	8.13 8.66 7.12	1.99 2.36 2.22
41	Office	P0-P6	ODOM* SLAM	3.51 3.36	16.02 14.84	2.71 2.49
42	OldBrick-HouseDay	P1-P2 P3* P4-P7	ODOM* ODOM SLAM	1.74 1.54 1.29	11.15 11.80 7.76	1.48 1.25 1.10
43	OldBrick-HouseNight	P1*, P2 P4-P7	ODOM* ODOM SLAM	1.83 1.68 1.59	16.07 16.35 13.05	1.53 1.56 1.50
44	Old-IndustrialCity	P0-P9	ODOM SLAM	2.25 1.58	8.60 7.20	4.33 3.76
45	Old-Scandinavia	P1-P6	ODOM* SLAM	2.22 2.15	11.68 11.47	8.90 8.38
46	OldTownFall	P0*, P1* P2	ODOM* ODOM SLAM	1.62 1.25 0.75	6.44 4.09 2.47	1.53 0.11 0.28
47	OldTownNight	P0-P2	ODOM SLAM	0.83 0.61	4.74 3.49	1.24 0.95
48	OldTown-Summer	P0-P2	ODOM SLAM	2.42 2.41	11.90 11.84	1.57 1.54
49	OldTown-Winter	P0-P2	ODOM SLAM	0.60 0.53	2.14 2.33	0.72 0.75
50	PolarSciFi	P0-P8	ODOM SLAM	2.76 2.68	12.74 12.34	2.19 2.18
51	Prison	P0-P11	ODOM SLAM	4.14 4.12	21.37 20.78	4.59 4.68
52	Restaurant	P1-P8	ODOM SLAM	1.51 1.03	10.99 8.00	0.97 0.70
53	RetroOffice	P0-P5	ODOM SLAM	1.14 0.94	3.11 2.85	0.10 0.09
54	Ruins	P1-P6 P8-P9	ODOM SLAM	3.07 3.05	16.68 17.07	9.43 9.09
55	SeasideTown	P0-P7	ODOM SLAM	0.67 0.61	1.79 1.58	0.56 0.44
56	SeasonForest-Autumn	P0-P2	ODOM SLAM	5.41 5.10	35.20 31.76	21.38 18.73
57	SeasonForest-Spring	P0-P3	ODOM SLAM	4.09 3.93	25.14 28.30	15.03 15.02
58	SeasonForest-SummerNight	P0-P1	ODOM SLAM	3.65 3.45	21.45 19.42	25.05 23.00
59	SeasonForest-Winter	P0-P2	ODOM SLAM	6.73 7.53	30.59 32.61	15.47 19.11
60	SeasonForest-WinterNight	P0-P2	ODOM SLAM	4.77 5.14	30.45 30.09	27.40 26.31
61	Sewerage	P1-P11	ODOM SLAM	3.94 3.87	30.11 27.64	6.74 5.92
62	ShoreCaves	P1-P8	ODOM SLAM	1.86 1.77	7.56 7.20	3.41 3.00
63	Slaughter	P0, P1* P2-P10 P11*	ODOM* ODOM SLAM	4.52 3.97 3.80	26.89 27.19 24.49	6.04 5.53 5.34
64	SoulCity	P0*, P1, P2* P3-P4, P5* P6, P7	ODOM* ODOM SLAM	5.22 4.74 4.82	32.59 28.79 29.27	7.30 7.96 8.10
65	Supermarket	P0*, P1, P2 P3*, P4-P6	ODOM* ODOM SLAM	4.70 4.82 4.73	23.19 22.64 23.38	3.69 3.66 3.60
66	Terrain-Blending	P1, P3-P4	ODOM SLAM	0.45 0.55	1.65 1.90	1.31 1.55
67	Urban-Construction	P0-P4	ODOM SLAM	0.35 0.31	1.76 1.50	1.30 1.24
68	VictorianStreet	P0-P7	ODOM SLAM	0.99 0.72	4.67 3.17	0.43 0.25
69	WaterMillDay	P1-P3, P6	ODOM SLAM	0.48 0.30	2.54 1.12	0.74 0.59
70	WaterMillNight	P0-P6	ODOM SLAM	0.34 0.29	0.94 0.92	0.78 0.72
71	Western-DesertTown	P1-P7, P9 P11, P13	ODOM SLAM	1.89 1.78	13.77 12.97	8.09 7.32